Progress In Electromagnetics Research C, Vol. 75, 203–217, 2017

A Scalable Compact Wideband Dual-Polarized Printed Dipole Antenna for Base Station Applications

Chengcheng Tang[1, 2, *], Huy Cao[1, 3], and Jimmy Ho[1]

Abstract—A novel compact wideband dual-polarized printed dipole antenna for base station application is presented. The proposed antenna is composed of four assembled substrates. Two pairs of identical arrow-shaped conductive lines on the tophat substrate form two orthogonal polarized dipoles. Two baluns connected with 50 Ω coaxial cables are integrated on another two vertical substrates to excite the dipoles. The other horizontal board at bottom provides grounding. A rectangular box-shaped reflector is also used to enhance its stability in radiation patterns over the operating frequencies. It achieves 22% size reduction from the conventional printed half-wavelength cross-dipole, and 43.2% impedance bandwidth (VSWR < 2), while maintaining a stable radiation pattern with measured Cross-Polarization Degradation (XPD) better than -22 dB at boresight and an average peak gain of 8.4 dBi for a 65° Azimuth Beamwidth base station application at 700/800/900 MHz bands. With the scalable miniature structure, it may also find itself suitable for side-by-side multiband Multi-Input Multi-Output (MIMO) or Large-Scale Antenna (LSA) 5G base station applications. A 4×4 array prototype of the LSA is also designed and fabricated, and it achieves 27.8% impedance bandwidth (VSWR < 1.5) with well decorrelated element performance and array XPD better than -20 dB across as large as 30° tilting range.

1. INTRODUCTION

Dipole antennas have been widely used in base stations because they are capable to have a dual-polarized structure, which can provide polarization diversity to reduce the side effects of multipath fading and to increase channel capacity [1]. Meanwhile, they can also achieve a wider bandwidth with simpler structure compared with dual-polarized patch/slot antennas [2]. In order to further improve the impedance bandwidth of the dual-polarized dipole antennas, many efforts have been done [3–5], while very few attention has been paid on optimizing the dimension of the dual-polarized dipole antennas for base station have been reported, especially for those printed dipole antennas [6–8], which are commonly used in industry due to their outstanding features in terms of simple structure, light weight and low cost, but good performance. However, the physical height of these printed dipole antennas usually exceeds $0.25\lambda_0$ (λ_0 is the free-space wavelength at the central operating frequency), and the transverse overall length exceeds $0.5\lambda_0$, which makes it difficult to be deployed in a size limited antenna application, e.g., multi-band side-by-side configuration or LSA, which requires even smaller adjacent spacing ($0.5\lambda_0$ Vs. $0.75\lambda_0$ of conventional 10° down tilt antenna) for the large 3D beamforming tilting range to achieve the boost of overall system's capacity. Recently, several compact wideband dipole antennas have been reported in [9–11]. Liu in [9] used a square patch director and an octagon ring as a parasitic element on top of the dual-polarized cross dipole to improve the bandwidth, as well as to achieve a size reduction. However, this stacked structure sacrifice the height of the antenna and make it even taller as $0.32\lambda_0$. Wu in [10] applied a beveled offset feeding structure to broaden the impedance bandwidth, and also

Received 15 May 2017, Accepted 3 July 2017, Scheduled 17 July 2017

* Corresponding author: Chengcheng Tang (richard.tangcc@gmail.com).

[1] Amphenol Antenna Solutions, Inc. 1123 Industrial Dr. SW, Conover, NC 28613, USA. [2] CommScope, Inc. 2601 Telecom Pkwy, Richardson, TX 75082, USA. [3] Kathrein USA, 2400 Lakeside Blvd #650, Richardson, TX 75082, USA.

achieve a compact size, while it is difficult to be realized in dual-polarized base station antennas due to the specific beveled feeding structure required.

More specifically, a comparison on the transvers length L, physical height H and bandwidth of a printed dipole with integrated balun (antenna A) [6], a size-reduced printed dipole with triangular patch (antenna B) [11] and the proposed antenna C are listed in Table 1. It can be observed that all of them achieved wide impedance bandwidth over 40% (VSWR < 2). Although antenna B achieves 19.5% shorter than antenna A, its transverse size is still large, only about 7% improvement over antenna A is achieved. Consequently, even the size reduced antenna B may face the problem of size limit, especially for compact antenna arrays in the massive-MIMO or LSA. While the proposed antenna C achieves 22% transverse size reduction over antenna A with a similar height as antenna B. Nowadays, more and more attention has been paid to realize the base station antennas covering separate bands centered at 800 MHz (690–960 MHz) as LB and 2200 MHz (1710–2690 MHz) as HB, and/or 3500 MHz for LTE and 5G applications in the same antenna package. There are two commonly used embodiments for such an antenna array design. One is using coaxially settled interleaved LB and HB elements [12], which has a narrower overall antenna width but may sacrifice performance like the bandwidth, isolation and radiation pattern, and the other is using side-by-side LB and HB elements. Compared with the LB element in [12], which has a $0.64\lambda_0$ transvers length and 23.5% impedance bandwidth, the proposed antenna C has much smaller dimension and 19% more impedance bandwidth. Due to its miniature dimension, the proposed antenna may find itself better candidate for the side-by-side configuration for LTE and massive MIMO or LSA for the coming 5G applications.

Table 1. Comparisons of Antenna A, Antenna B and Antenna C.

	L_a, L_b, L_c	H_a, H_b, H_c	*Impedance Bandwidth*
Antenna A	$0.504\lambda_0$	$0.294\lambda_0$	41% (VSWR < 2)
Antenna B	$0.47\lambda_0$	$0.246\lambda_0$	46.8% (VSWR < 2)
Antenna C	$0.39\lambda_0$	$0.25\lambda_0$	43.2% (VSWR < 2)

λ_0 is the free-space wavelength at the central operating frequency.

This paper is organized as follows. In Section 2, a novel compact wideband dual-polarized printed dipole antenna unit is designed for 700 MHz to 900 MHz (antenna C), with its equivalent-circuit and performance discussed. In Section 3, antenna C is successfully scaled to a higher frequency band (antenna D) to build a 4×4 array prototype of the LSA, with the array performance analyzed. Finally, some conclusions are presented in Section 4.

2. DUAL-POLARIZED COMPACT DIPOLE FOR ULTRA LOW BAND

2.1. Antenna Element

The geometry of the proposed antenna designed for Ultra Low Band (690 MHz–960 MHz) base station application (Antenna C) is shown in Fig. 1, with the optimized geometry parameters by HFSS [13] shown in Table 2, for an operation with the center frequency at around 825 MHz. Basically, the antenna consists of two pairs of identical arrow-shaped conductive lines etched horizontally on the tophat substrate (FR4 with thickness $T_{\text{top}} = 0.762$ mm) to form two orthogonally ($\pm 45^\circ$) polarized dipoles; and two baluns consist of multi-section impedance transformer connected with 50 Ω coaxial cables integrated on the other two vertical substrates (Arlon 25N with thickness $T_{\text{balun}} = 1.524$ mm) perpendicular to the tophat radiator, to excite the dipole antenna; another rectangular printed circuit board (PCB) (Arlon AD255C with thickness $T_{\text{base}} = 1.524$ mm) as the base to provide the ground. Different PCB materials are used due to cost and Passive Intermodulation (PIM) optimization. A square box-shaped aluminum reflector is also used to enhance its stability in radiation patterns over the operating frequencies, including the XPD improvement and Azimuth 3-dB beamwidth control. More specifically, as shown in Fig. 1(c), the tophat PCB comprises four identical quadrants of arrow-shaped conductive lines, with the first and third quadrants associated with the first polarization, and the second and fourth quadrants associated

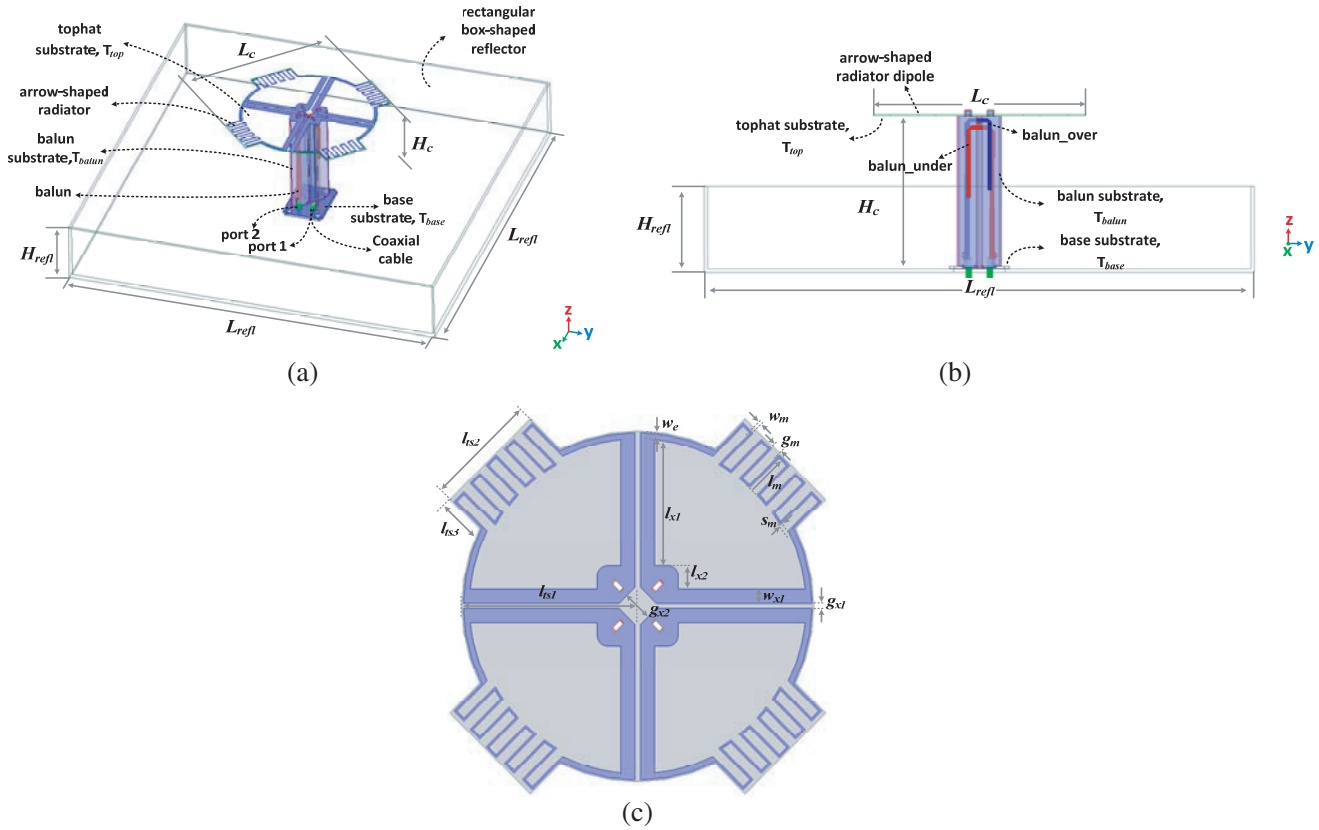

Figure 1. Geometry of the proposed dual-polarized Antenna C element: (a) 3D view; (b) Side view; (c) Perspective view of arrow-shaped meander line radiator.

with the second polarization. Each quadrant comprises conductive straight lines on two edges, with the width w_{x1}, and length l_{x1}, and a rounded square pad in the junction of the two straight lines with the equal width and length l_{x2} is for soldering the top radiator to the back side (ground side) of the vertical baluns. The quadrant also has a radially extended portion, which has a shape of rectangular slantly positioned with tangential length l_{ts2} and normal width l_{ts3}. It comprises a meander line component with number of loops $n = 5$, the width of meander line w_m, the length of the meander line in tangential section g_m and in normal section l_m, and the width of the curved conductive lines on edge w_e.

2.2. Mechanism Analysis and Parameter Study

To better understand the mechanism of antenna C, further analysis on the radiator has been done as follows.

Figure 2 depicts the current distribution of the dipole radiator at 825 MHz when port 1 is excited. It can be seen that the current flowing conformably along the $+45°$ direction to form the familiar cosine current distribution of a half-wavelength dipole from the feed point in the center to the middle of the meander line components through two identical paths in parallel. The meander line consists of several loops that are closely grouped and configured in such a way that the overall size of each quadrant is significantly reduced but still able to satisfy electrical length needed to function as a quarter-wavelength arm conductor of a half-wavelength dipole. As a result, the overall size of the radiator is reduced as well. It can also be clearly observed that the current on the straight conductive lines of the two quadrants in $+45°$ direction is coupled by the straight conductive lines of the other two quadrants in $-45°$ direction, which contributes to broaden the impedance bandwidth. It seems that the straight conductive lines of the four quadrants in the middle form coupled lines with a gap g_{x1}, contributing to the first resonance with frequency as f_1. The meander line components plus the straight conductive lines provide another

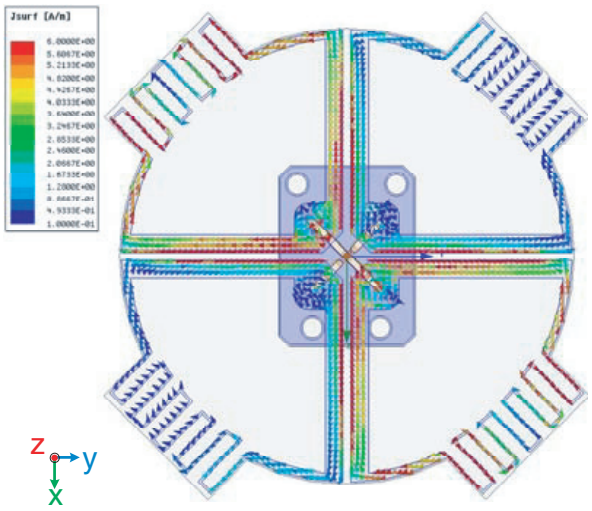

Figure 2. Current distribution of the Antenna C radiator at 825 MHz (port 1 is excided).

resonance with frequency as f_2.

Due to the symmetrical structure, the simplified equivalent circuit of only one quadrant of the dipole radiator with the meander line components is illustrated in Fig. 3 based on the coupled line equivalent circuit and the broadband equivalent circuit model from Tang et al. [14] used for both straight line dipole antenna (SLDA) and meander line dipole antenna (MLDA). It can be seen that the coupled lines with one end loaded and the other end open, forms a low pass filter (LPF) equivalent circuit, with the lumped elements L_{11}, C_{11} and R_{11}, in series with the equivalent circuit model of the MLDA. The two identical current flowing paths in Fig. 2 also indicates a parallel overall connection.

In order to verify the accuracy of the derived equivalent circuit model, as well as a better understanding of how the dimensions of the dipole radiator affect its performance, some key parameters of the radiator, which are related to the strongest current locations in the current distribution shown in Fig. 2, have been selected to be studied in simulation. For simplicity, only port 1 is excited with S_{11} be studied for impedance matching. When one parameter is studied, the others are kept constant as in Table 2.

Table 2. Parameters for Antenna C.

Parameters	L_c	H_c	g_{x1}	g_{x2}	w_{x1}	l_{x1}
Values (mm)	137.1 ($0.39\lambda_0$)	88.4 ($0.25\lambda_0$)	1.99 ($0.006\lambda_0$)	9.9 ($0.025\lambda_0$)	4.49 ($0.013\lambda_0$)	41.7 ($0.12\lambda_0$)
Parameters	l_{x2}	w_e	l_{ts1}	l_{ts2}	l_{ts3}	w_m
Values (mm)	7.82 ($0.022\lambda_0$)	2.25 ($0.006\lambda_0$)	57.77 ($0.16\lambda_0$)	43.19 ($0.12\lambda_0$)	14.99 ($0.04\lambda_0$)	0.62 ($0.001\lambda_0$)
Parameters	g_m	s_m	l_m	w_a	l_a	w_b
Values (mm)	4 ($0.011\lambda_0$)	0.15 ($4e-4\lambda_0$)	13.7 ($0.039\lambda_0$)	4.19 ($0.012\lambda_0$)	49.66 ($0.14\lambda_0$)	3.69 ($0.011\lambda_0$)
Parameters	l_b	w_c	w'_a	l'_a	w'_b	l'_b
Values (mm)	22 ($0.063\lambda_0$)	4.49 ($0.013\lambda_0$)	4.39 ($0.013\lambda_0$)	29.18 ($0.083\lambda_0$)	3.69 ($0.011\lambda_0$)	30 ($0.085\lambda_0$)
Parameters	w'_c	l'_c	w'_d	l'_d	l'_o	w'_o
Values (mm)	4.49 ($0.013\lambda_0$)	16.24 ($0.046\lambda_0$)	2.43 ($0.007\lambda_0$)	7.2 ($0.021\lambda_0$)	47.57 ($0.14\lambda_0$)	2.43 ($0.007\lambda_0$)

λ_0 is the free-space wavelength at the central operating frequency.

2.2.1. Effect of the Straight Conductive Lines

The first key parameter studied is the gap g_{x1}, which is formed by the straight conductive lines in the middle section of the dipole radiator, to affect the performance of the equivalent coupled line LPF. Fig. 4(a) shows the simulated results of the return loss versus different g_{x1}. It can be observed that when the gap g_{x1} is reduced, the capacitance C_{11} shown in Fig. 3 is increased, the higher resonant frequency f_1 gets lower, which ties up with its equivalent LPF circuit. The width of the *conductive lines' effect on the return loss is also studied and shown in Fig. 4(b). The change of the width* w_{x1} would affect both the inductance L_{11} and capacitance C_{11} according to the theory of coupled transmission lines, which would also affect both the higher resonant frequency f_1 from the coupled lines effect and lower resonant frequency f_2 from the effect of overall radiator. It can be seen that when w_{x1} is increased, the higher

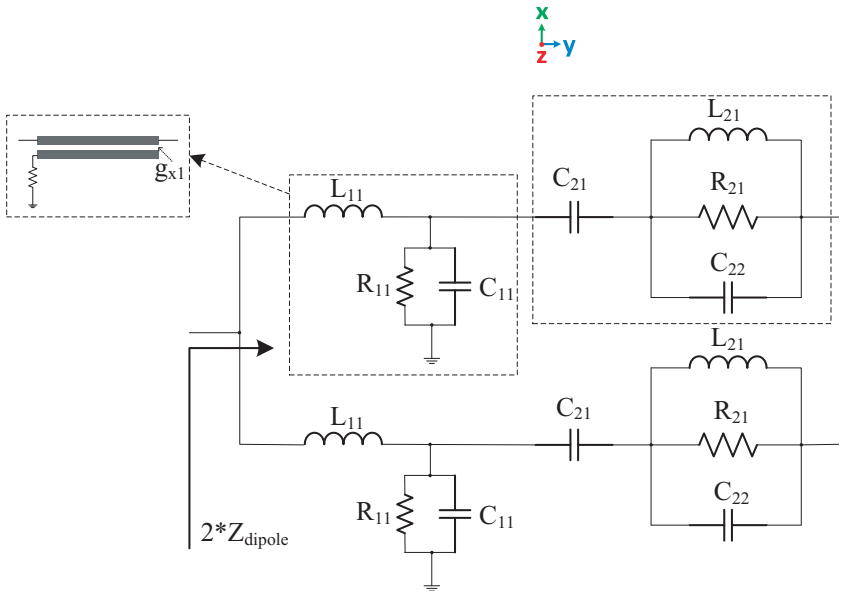

Figure 3. Simplified equivalent circuit of antenna C's dipole radiator.

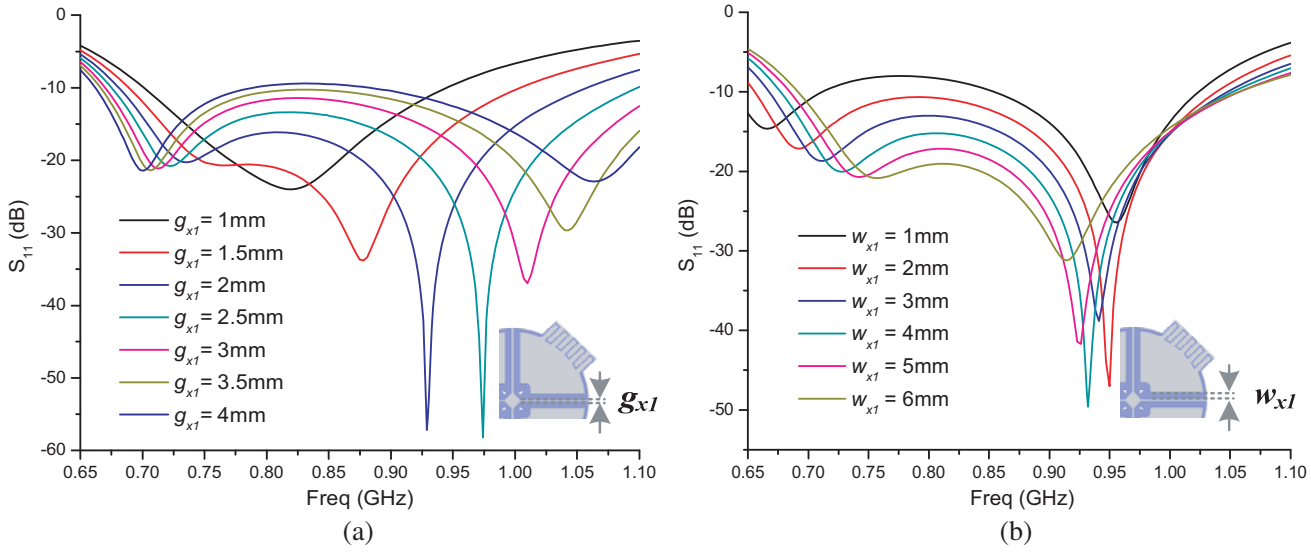

Figure 4. Effect of straight conductive lines on return loss: (a) Return loss of Port 1 versus different g_{x1}; (b) Return loss of Port 1 versus different w_{x1}.

resonant frequency f_1 gets lower and the lower resonant frequency f_2 gets higher, which also ties up with the equivalent circuits shown in Fig. 3. According to Fig. 4(a), when $g_{x1} = 3\,\text{mm}$, the proposed antenna can achieve a simulated impedance bandwidth of 50.2% ranging from 0.67 GHz to 1.12 GHz for return loss $< -10\,\text{dB}$, with the antenna's transverse length as $0.39\lambda_0$ and height as $0.25\lambda_0$, which shows 22% and 17% reduction on the overall size compared with the Antenna A and Antenna B in Table 1 separately, but achieving a better impedance bandwidth.

2.2.2. Effect of the Meander Line Components

The other important parameters studied are the horizontal gap between the meander line component g_m and the vertical length of the meander line component l_m. The simulated return loss results are shown in Figs. 5(a) and (b) for different g_m and l_m separately. It can be observed that basically the meander components mainly affect the lower resonant frequency f_2 only, and the larger the gap g_m is, the lower f_2 would be. Similarly, the longer the length l_m is, the lower f_2 is observed, which means that the meander components contribute mainly to the total electrical length of the radiator. Although meander line antenna technique has been widely used on mobile terminals for size reduction, it has seldomly been reported on dipole antenna for base station. According to the above results, the proposed antenna achieves a significant transverse size reduction while maintain a similar impedance bandwidth thanks to the meander line components.

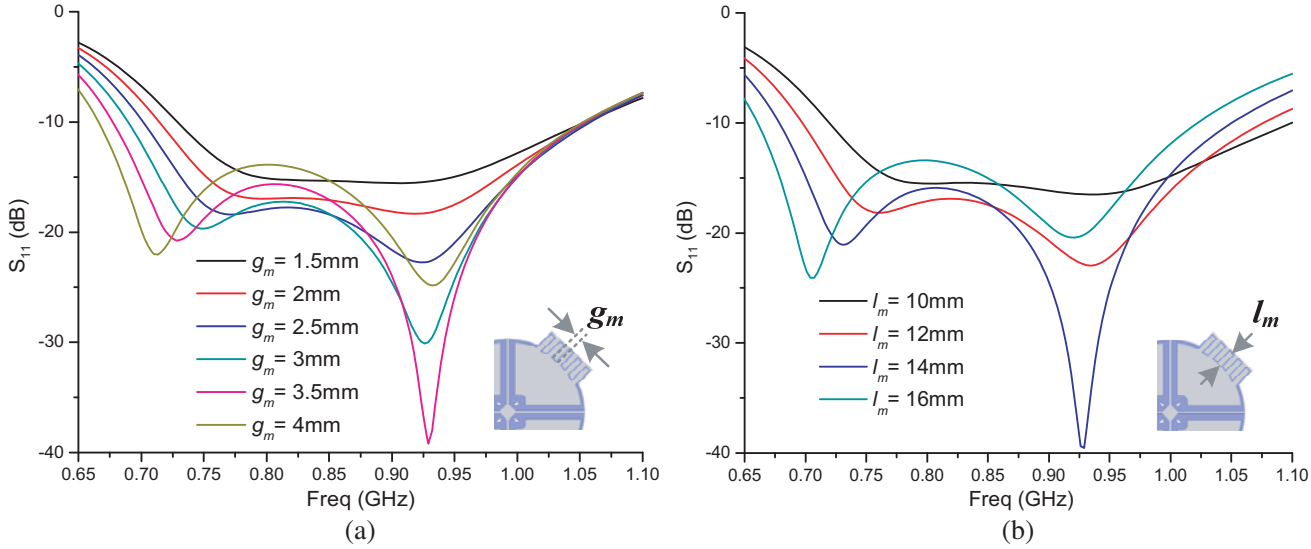

Figure 5. Effect of meander line components on return loss: (a) Return loss of Port 1 versus different g_m; (b) Return loss of Port 1 versus different l_m.

2.3. Results and Discussions

To validate the design, a prototype of the proposed dual-polarized dipole antenna, which is optimized for LTE700/800/900 MHz bands, is fabricated and illustrated in Fig. 6. Fig. 7 shows the simulated and measured VSWRs and gains for the two ports of Antenna C. Because of the different structures in baluns, the two ports are observed slightly different in response. It can be seen that although the measurement slightly deviates from the simulation due to the fabrication errors and test environment, the measured and simulated VSWRs and gains are in good agreement in terms of the overall response trend. The measured impedance bandwidth ranges from 0.67 GHz to 1.04 GHz (43.2%) for VSWR < 2 or from 0.685 GHz to 1.0 GHz (37.3%) for VSWR < 1.5, which is wide enough for the base station applications covering all the mainstream LTE700/800/900 MHz bands. The simulated gain is stable across the frequency band, while the measured gain is slightly degraded from simulation results, but

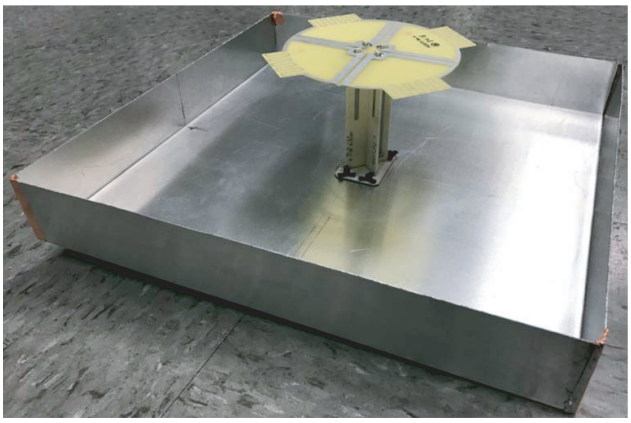

Figure 6. Photograph of fabricated Antenna C.

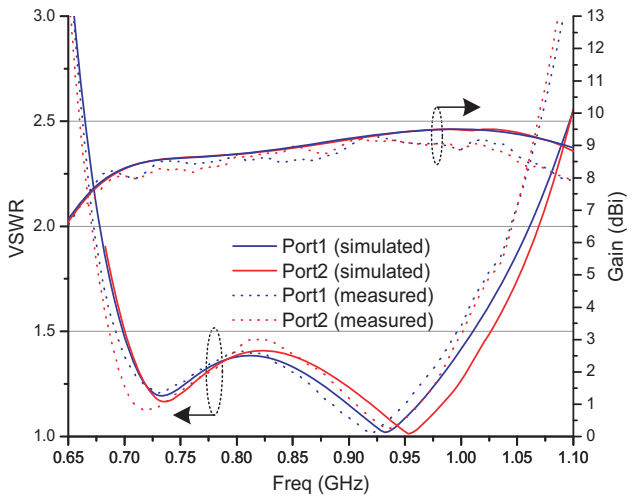

Figure 7. Simulated and measured VSWRs and gain of Antenna C.

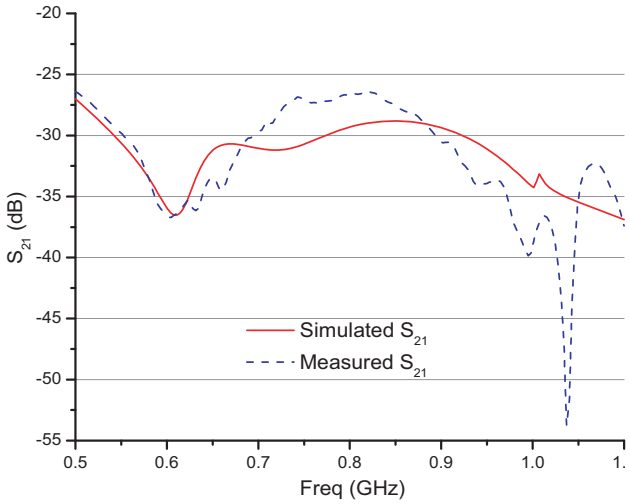

Figure 8. Simulated and measured port to port isolation of Antenna C.

still acceptably stable with measured value of 8.6 ± 0.6 dBi based on BASTA [15] calculation for the operating frequency bands from 0.69 GHz to 0.96 GHz.

The simulated and measured port-to-port isolations S_{21} are shown in Fig. 8. Similarly, due to the fabrication errors and test environment, the measurement and simulation results are different, but they agree with each other in terms of the overall response trend. It has a measured port-to-port isolation as a single element better than -25 dB across the whole operating band, which fulfills the industrial requirement.

The radiation pattern measurement is done with the Satimo Stargate 64 Anechoic Chamber, and Fig. 9 shows the simulated and measured radiation patterns of the proposed Antenna C in both Azimuth (Az-) plane and Elevation (Elv-) plane at frequencies of 0.69 GHz, 0.825 GHz and 0.96 GHz for port 1 ($+45°$-pol). Due to the symmetrical structure of the antenna, there is only a slight difference in the radiation patterns for both ports, so only the results for port 1 are shown. As shown in Fig. 9, the simulated and measured radiation patterns tie well up with each other in Co-pol for both Az- and Elv-planes across the operating frequency band. The measured X-pol gets a little bit degraded than the simulation and it may be caused by the fabrication errors and test environment. The measured Azimuth 3-dB beamwidth reads as $65.8°$, $60.1°$, and $56.2°$ for 0.69 GHz, 0.825 GHz and 0.96 GHz respectively. The measured XPDs at boresight for both Az- and Elv-planes are less than -22 dB. The measured front-to-back ratios remain over 27 dB and change slightly with frequency.

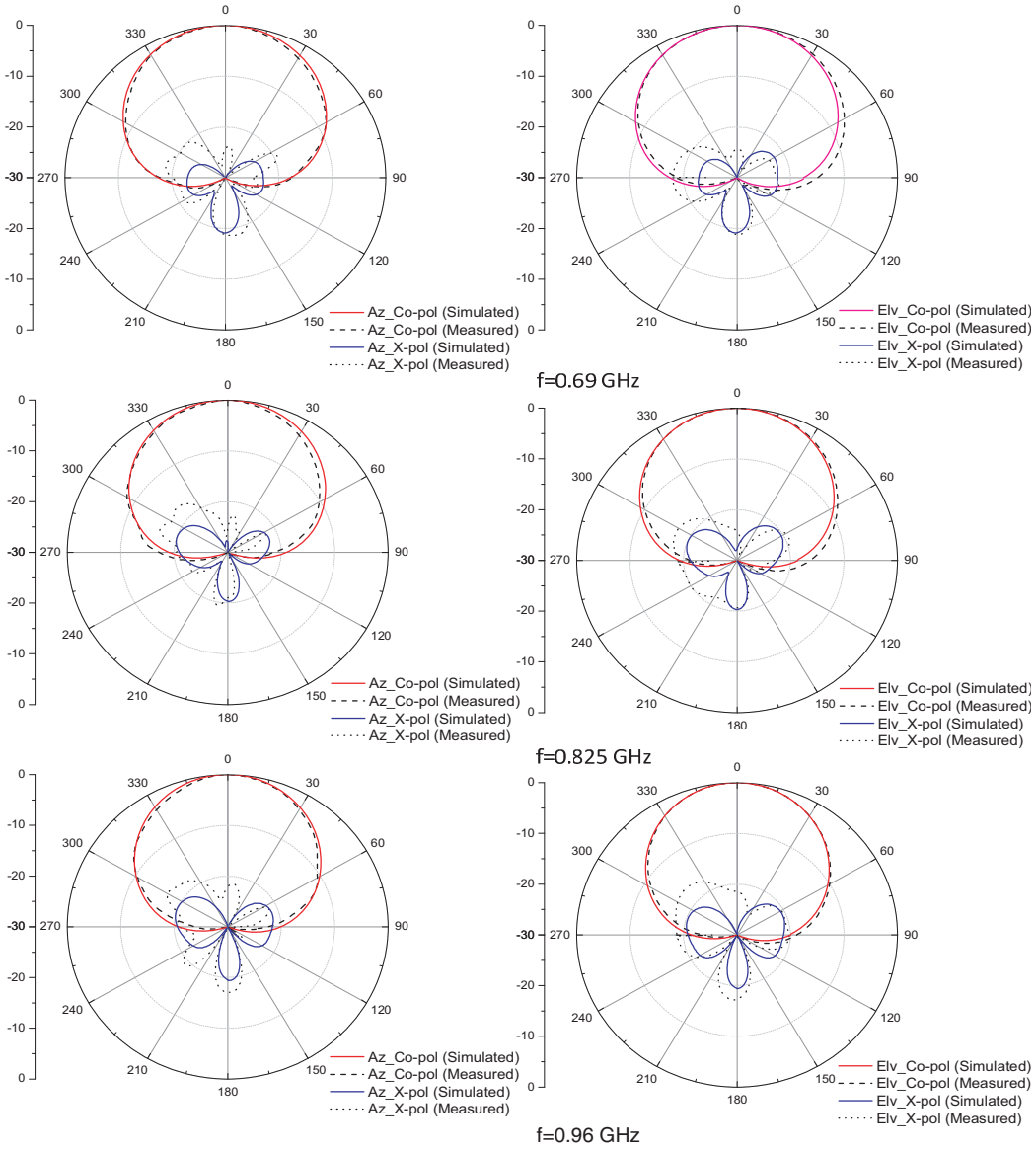

Figure 9. Simulated and measured radiation patterns of Antenna C at 0.69 GHz, 0.825 GHz and 0.96 GHz when port 1 is excited (+45°-pol).

3. DOWN-SCALED COMPACT DIPOLE FOR LSA APPLICATION

Due to the significant overall size reduction achieved, the proposed antenna may find itself a good candidate for the potential base station 5G massive MIMO antenna array or LSA applications. The massive MIMO or LSA requires relatively smaller spacing between the adjacent elements than the traditional passive antenna array, e.g., close to half-wavelength spacing in the massive MIMO antenna array or LSA array Vs. 3/4 wavelength spacing in a traditional 10-deg down tilt passive antenna array, for the achievement of a larger tilting angle, e.g., 30° without running into grating lobe issue for the beamforming realization, which is an advanced performance in 5G technology over the current passive antenna array. The traditional radiating elements, including but not limited to the half-wavelength dipole and patch antenna element may either not mechanically fit for such small spacing structure or have severe mutual coupling among adjacent elements to degrade the port-to-port isolation of single element and the XPD of the array radiation pattern, as well as to reduce the corresponding capacity

of overall system due to such correlated antenna elements in MIMO array [16]. In addition, the patch radiating element in such a restricted spacing array usually suffers from the narrow bandwidth. Antenna D, which is a down-scaled version of Antenna C, is designed and optimized to cover Band 41 and Band 42 (3.3 GHz–3.9 GHz), part of low Super High Frequency (SHF) for a potential 5G application in the future. Then a 4×4 array prototype of LSA consist of Antenna D with 46 mm ($0.5\lambda_l$ at lower end of operating frequency band) spacing between the adjacent elements is fabricated and tested.

3.1. Antenna Element

The geometry of the down-scaled version of Antenna C is shown in Fig. 10, which is named Antenna D here. As shown in Fig. 10(a), there is a feeder board with two 50 Ω-transmission lines feeding port 1 and port 2 of Antenna D, respectively, because the dimension of Antenna D is too small to apply the direct coaxial cable feeding. Basically, the overall dimension of Antenna D is directly down-scaled from Antenna C with the scale factor $f_{\text{scale}} = 0.248$, only with some parameters optimized for the 3.5 GHz band and they are listed in Table 3. Due to the very small dimension of Antenna D, the PCB substrate thickness gets reduced from what has been used for Antenna C for a purpose of reducing cost, with a potential sacrifice on narrower impedance bandwidth due to narrower transmission lines. The tophat substrate (FR4) has a thickness $T_{\text{top}}\_d = 0.254$ mm, and the two vertical balun substrates (Arlon 25N) have a thickness $T_{\text{balun}}\_d = 0.508$ mm. The feeder board substrate has a thickness $T_{\text{base}}\_d = 0.508$ mm as well. A square box-shaped aluminum reflector with length $l_{\text{refl}}\_d = 46$ mm ($0.55\lambda_0$) and height $h_{\text{refl}}\_d = 13.5$ mm ($0.16\lambda_0$) is also used to achieve Azimuth 3-dB beamwidth control. As shown in Fig. 10(b), an extra T-shape component consists of a curved tangential line with width w_T_d and tapered normal line with wider width as w_{To}_d and narrower width as w_{Ti}_d are added into each quadrant on the radiator, with the location l_T_d from the center. This T-shape component introduces an extra resonant frequency to be used for an enhancement of the impedance matching across the operating frequency. According to Fig. 11, which shows the current distribution of Antenna D radiator at 3.5 GHz when port 1 is excited, the dipole works the same as Antenna C does, but the T-shape component provides an extra path for the current, which could further improve the impedance matching for Antenna D. To validate it, Fig. 12 presents the simulated return loss of port 1 versus different locations of the T-shape component l_T_d with all the other parameters kept the same as listed in Table 3. It can be clearly observed that a third resonant frequency f3 appears on the higher end of the two original ones in Antenna C, which does not have the T-shape component, and only f_3 is dominated by the location of the T-shape component in such a way that f_3 gets lower when l_T_d gets larger, which means a longer

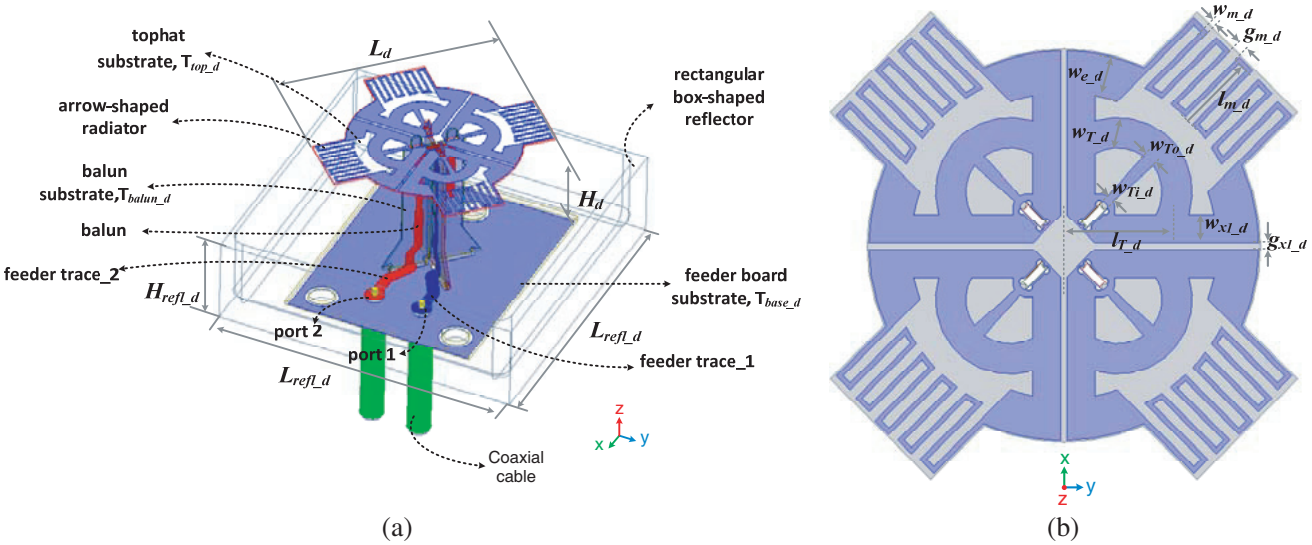

Figure 10. Geometry of the proposed dual-polarized Antenna D element: (a) 3D view; (b) Perspective view of arrow-shaped meander line radiator.

extra path for the current flowing would shift the resonant frequency f_3 lower. To achieve the maximum operating bandwidth with the optimized performance for the 3.5 GHz band, $l_T\_d = 7.13$ mm is chosen, with the simulated impedance bandwidth as 27.8% from 3.13 GHz to 4.14 GHz (VSWR < 1.5), which is significant improvement over those reported slot antenna [17] and Bowtie antenna [18] used in MIMO array.

Table 3. Some parameters for Antenna D.

Parameters	L_d	H_d	g_{x1_d}	w_{x1_d}	w_{e_d}	w_{T_d}
Values (mm)	34.09 ($0.39\lambda_0$)	21.49 ($0.25\lambda_0$)	0.43 ($0.005\lambda_0$)	1.83 ($0.021\lambda_0$)	2.95 ($0.034\lambda_0$)	2.17 ($0.025\lambda_0$)
Parameters	w_{Ti_d}	w_{To_d}	l_{T_d}	w_{m_d}	g_{m_d}	
Values (mm)	0.5 ($0.006\lambda_0$)	0.9 ($0.01\lambda_0$)	7.13 ($0.082\lambda_0$)	0.32 ($0.004\lambda_0$)	0.66 ($0.008\lambda_0$)	

λ_0 is the free-space wavelength at the central operating frequency.

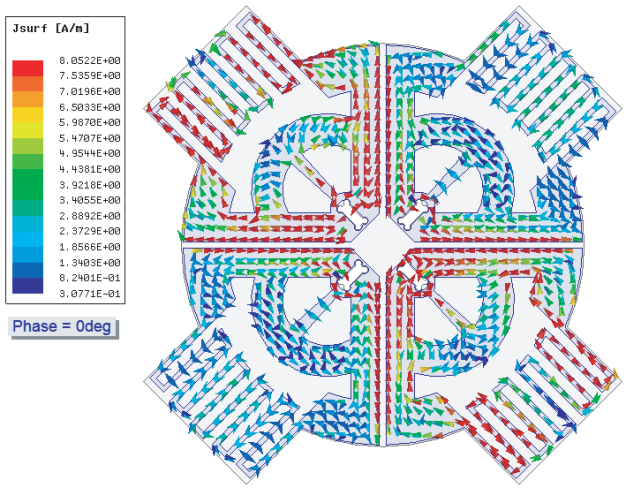

Figure 11. Current distribution of the Antenna D radiator at 3.5 GHz (port 1 is excided).

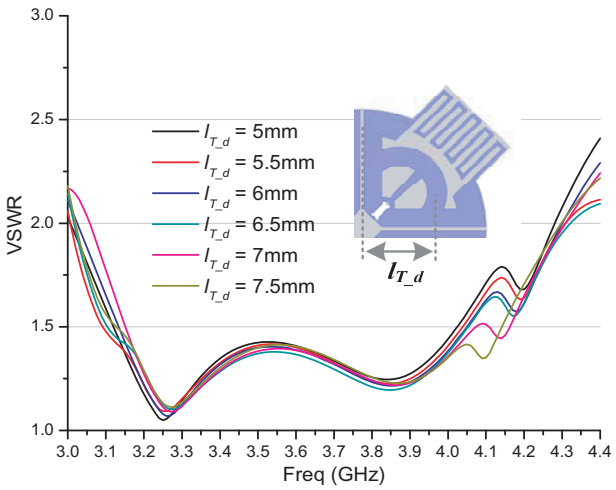

Figure 12. Simulated VSWRs of port 1 in Antenna D versus different l_{T_d}.

3.2. 4 × 4 Array Prototype of LSA

With the development of 4G LTE and future 5G technology, not only the planar MIMO antenna array is required on the mobile device, like the one described in [19], but also the massive MIMO antenna array is needed in the base station. To verify Antenna D as a good candidate for the massive MIMO antenna array or LSA for the future 5G base station applications, which requires smaller spacing between adjacent elements to realize a larger tilting range for the 3-D multiple beams beamforming, without degrading the isolation much, a 4×4 array prototype of LSA is fabricated with Antenna D, which is shown in Fig. 13. It is made up of four modules, each has a 2×2 sub-array, with an equal spacing between the adjacent elements inside the module ds_{inner} of 45.5 mm ($0.546\lambda_0$), and equal spacing between the elements in the adjacent modules ds_{outer} of 47 mm ($0.564\lambda_0$) as a 1 mm gap between the adjacent modules is required for practical product design. Because of the modular design, it can also be extended to $2n \times 2n$ LSA array.

One of the most challenging issues for the large tilting range of the LSA would be the mutual coupling effect caused by the very small element spacing. Such coupling would make elements in the MIMO become so correlated that it may not be able to obtain the diversity gain in the antenna system. In order to study the mutual coupling effect on different elements in different locations of the

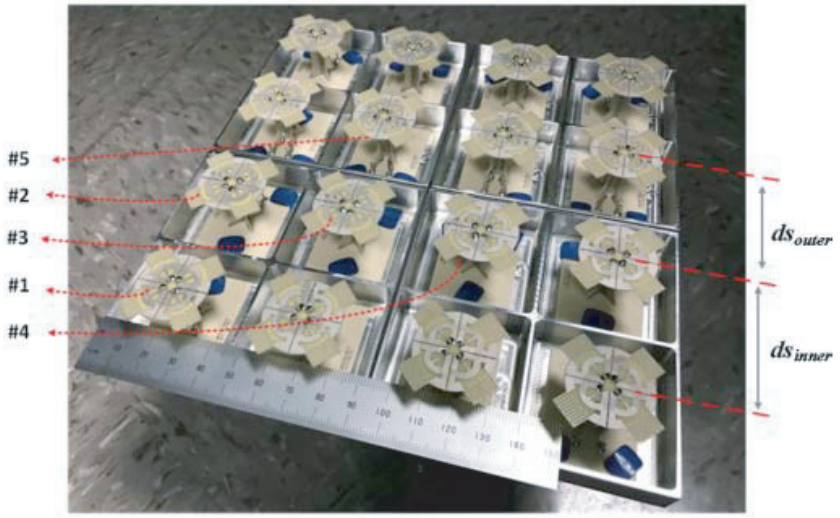

Figure 13. Photograph of the 4×4 antenna array.

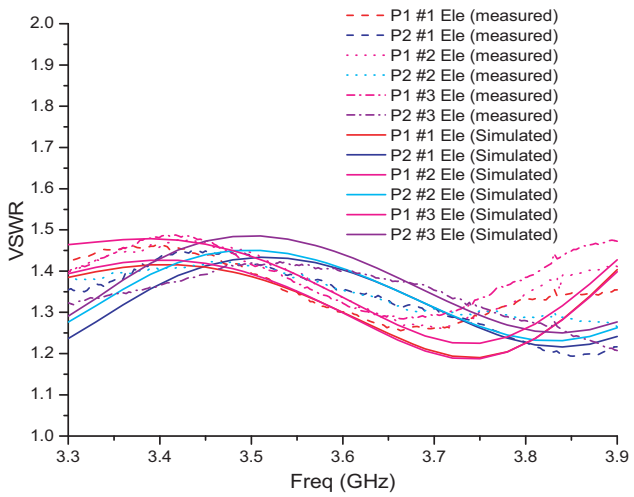

Figure 14. Simulated and measured VSWRs for both ports of the different elements #1 element at corner, #2 element on edge and #3 element in center.

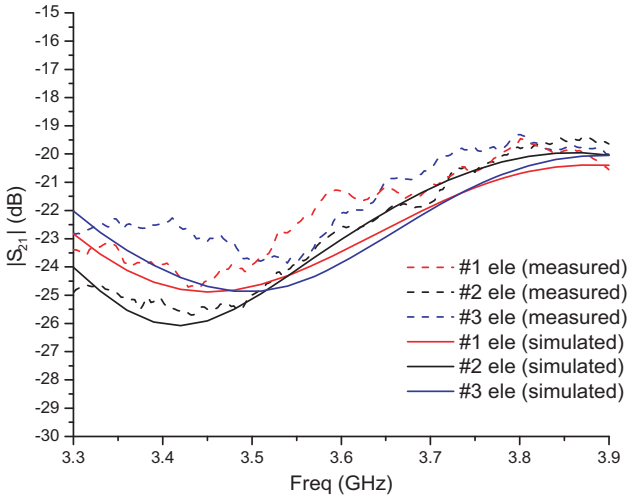

Figure 15. Simulated and measured port-to-port isolation for the different elements #1 element at corner, #2 element on edge and #3 element in center.

array caused by the very close element spacing, there are only three different elements, #1 #2 and #3 positioned in the corner, edge and center of the array respectively, been investigated in terms of VSWRs and port-to-port isolation due to the symmetrical structure of the 4×4 array. What's more, due to different relative locations of the element pair inside the array, another two elements #4 and #5 are also involved in the measurement of Envelop Correlation Coefficient (ECC), which shows the influence of different propagation paths of the RF signals that reach the antenna elements in a certain array structure. Fig. 14 shows the measured and simulated VSWRs of different elements in the array with all the other elements loaded with $50\,\Omega$ load. It can be seen that the measured results tie up well with the simulated ones, and different elements in different locations have quite similar VSWRs, with VSWR $\leq 1.5 : 1$ achieved for the whole operating frequency band. Fig. 15 depicts how the port-to-port isolation of a single element would be affected in different locations of the array. It can be seen that measured results match the simulated ones, with very minor different responses between different elements in the array. The measured port-to-port isolation for a single element in any position of the array is better than $-19\,\text{dB}$. Fig. 16 shows the measured approximated value of ECC based on the test

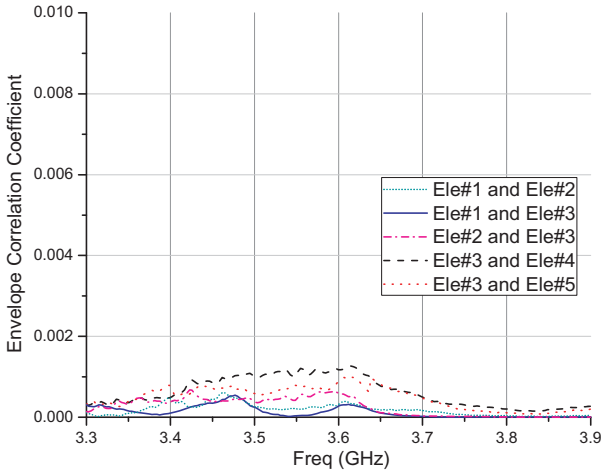

Figure 16. Measured results of envelope correlation for different elements in 4×4 array based on simple closed-form equation calculation in [20].

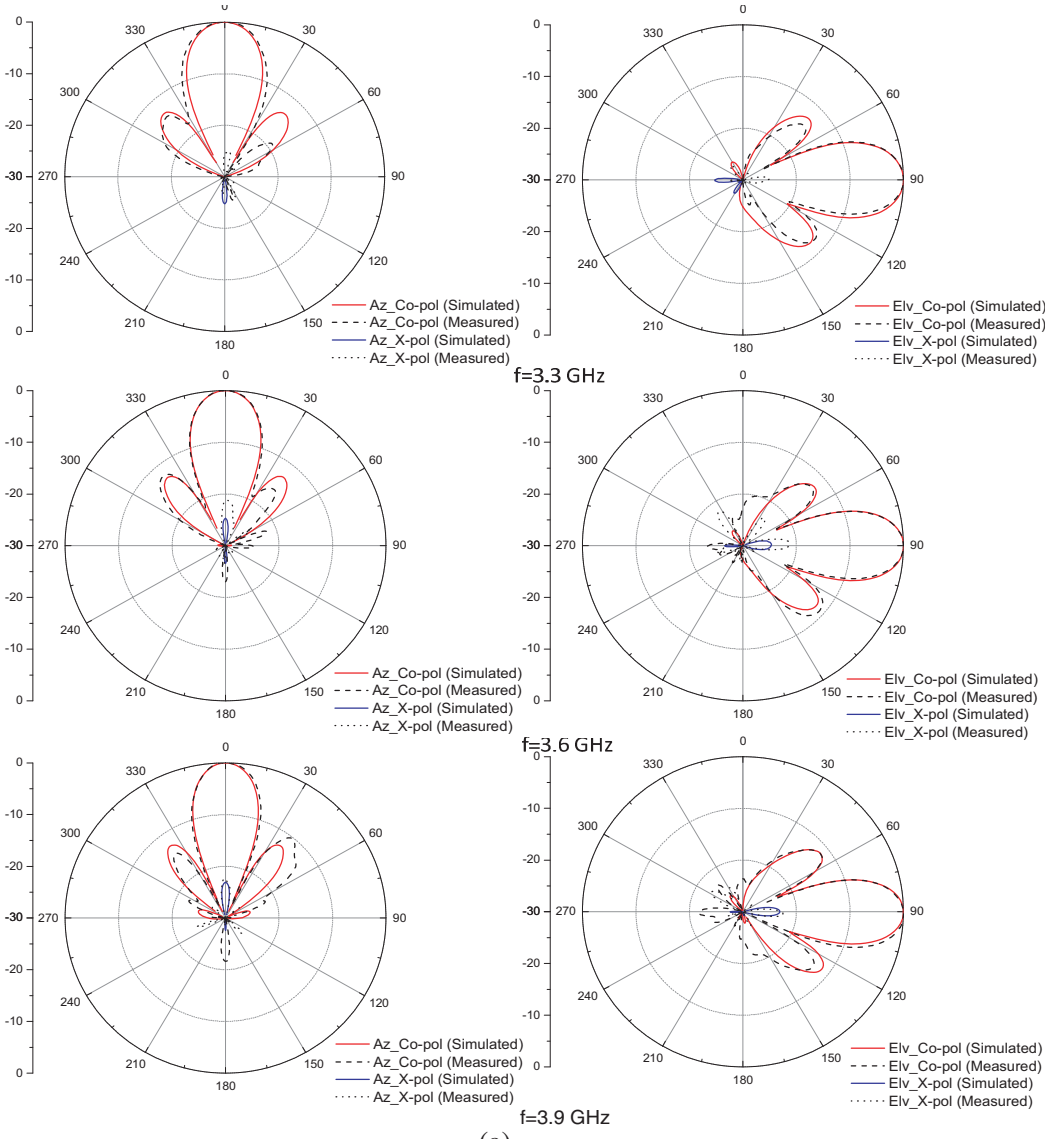

(a)

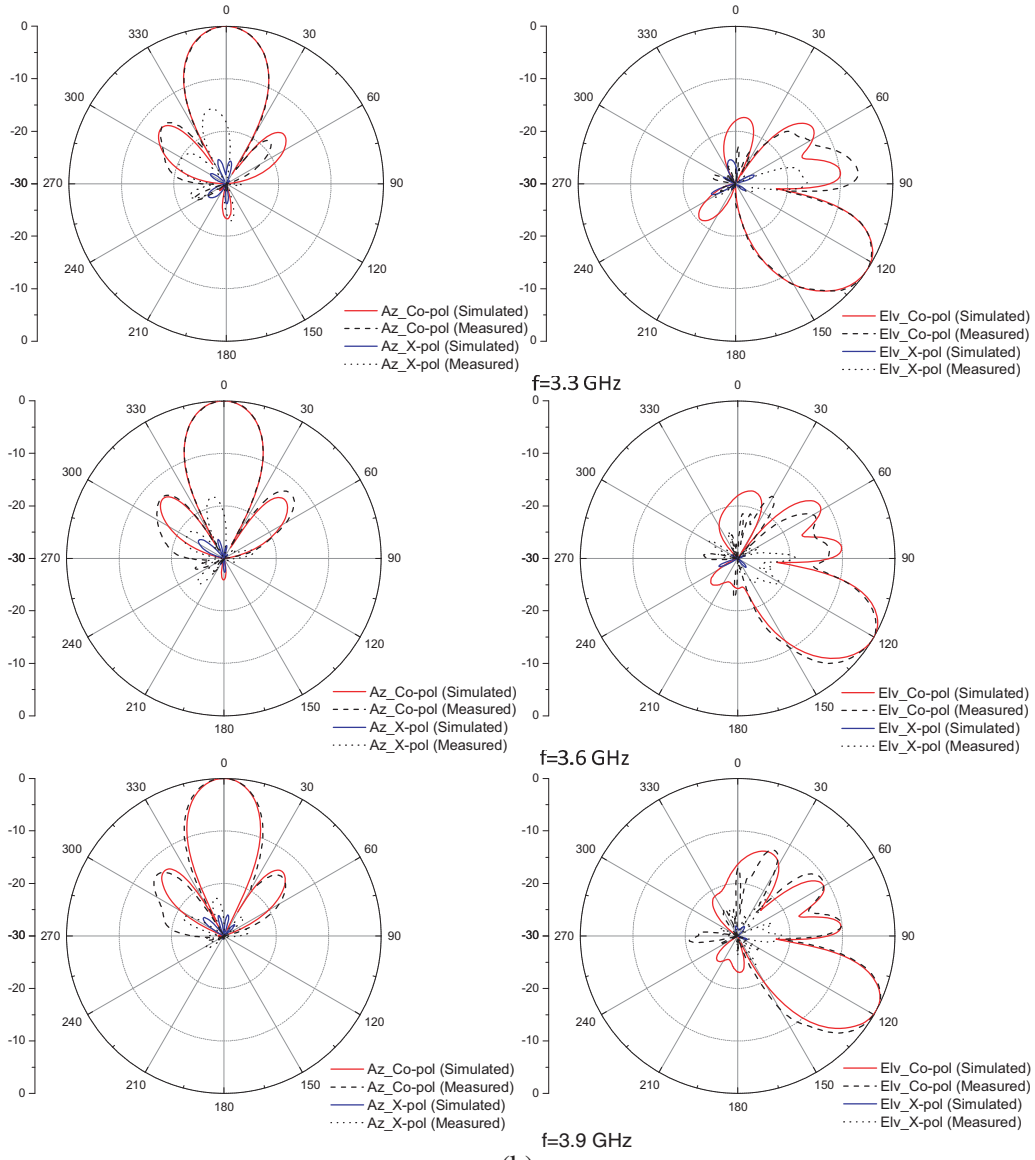

Figure 17. Simulated and measured radiation patterns of 4×4 array at 3.3 GHz, 3.6 GHz and 3.9 GHz with +45°-pol is excited for (a) 0° EDT; (b) 30° EDT.

procedure with a simple closed-form equation calculation using scattering parameters described in [20], which has been proved accurately and efficiently represents the performance of correlation of elements in the massive MIMO structure. It can be seen that physically further apart pair of elements has a smaller value of ECC, which means less correlated, while all of the tested pairs of elements have a very small value of ECC less than 0.002 over the whole operating frequency range, which is way lower than the industrial standard as 0.5 to obtain the diversity gain for the massive MIMO system [21], and even better than those narrow-band microstrip antennas utilizing decoupling technologies [22, 23]. Based on the results shown above, the mutual coupling does not affect much on the VSWRs and port-to-port isolation of the different elements in different locations in the LSA array, meanwhile the elements are well decorrelated in the proposed massive MIMO array, even though the element spacing is very small, which proves the proposed Antenna D as a better candidate for the small spacing LSA application than the traditional antenna elements, which could suffer from a significant degradation on the isolation and array performance when the element spacing is very small.

Moreover, the proposed massive MIMO planar array could be controlled with the genetic algorithms (GAs) described in [24, 25] to realize the optimized 3D beamforming by further eliminating interfering signals. However, in order to verify its measured radiation pattern in an easier way, a simple feeding network is applied to excite the 4×4 array for the radiation pattern measurement with the Satimo Stargate 64 Anechoic Chamber. Fig. 17 shows the simulated and measured $+45^\circ$ polarization radiation pattern of the 4×4 array in both Az- and Elv-planes and the -45° polarization radiation pattern should be quite similar due to the symmetrical structure of the element as well as the array. Figs. 17(a) and (b) show the radiation patterns at 0° Electrical Down Tilt (EDT) and 30° EDT respectively. It can be seen that the measured results and simulated results tie up well with each other, with minor difference due to fabrication error and test environment. Due to the fixed physical length of the feeding network, it achieves 28° to 32° tilting range for the frequency from 3.3 GHz to 3.9 GHz without grating lobe observed, which is twice of the traditional tilting range, with better than -20 dB and -18 dB measured XPD at boresight and 3dB respectively across the whole tilting range. The variation of the tilting range versus different frequencies can always be compensated by applying different progressive phase difference to different frequencies from digital beamforming technique in the future 5G application. What's more, in LSA application, different number of columns in the array can be excited together depends on different beamforming scenarios, e.g., in an 8×8 array can be divided into two halves, where 4 columns would be combined together, each one handles a 40 MHz carrier so that a total 80 MHz bandwidth could be achieved. In our case, due to the modular approach applied, it allows the 2×2 sub-array to be used to build any size of the LSA array according to the requirements of different applications.

4. CONCLUSION

A novel compact wideband dual-polarized printed base station antenna is presented in this paper. The antenna was composed of a horizontal tophat radiator, two vertical orthogonally positioned baluns, a base substrate at the bottom to support the dipole, and a rectangular box-shaped reflector. The proposed LB antenna achieved 22% overall size reduction over the traditional cross-dipole antenna, while maintaining 43.2% impedance bandwidth (VSWR ≤ 2) to cover the base station LTE700/800/900 bands, and stable radiation pattern with better than -22 dB XPD at boresight across the operating frequency band. A 4×4 array prototype of the LSA with the down-scaled version of the proposed antenna with impedance matching enhancement technique applied was also designed and fabricated. The array prototype achieves 27.8% impedance bandwidth (VSWR ≤ 1.5) to cover Band 42 and Band 43 in the future 5G applications, better than -19 dB port-to-port isolation of the individual elements in any location of the array, well decorrelated elements with all measured ECC less than 0.002 over the whole operating frequency range, 0° to 30° EDT range with better than -20 dB and -18 dB measured XPD at boresight and 3 dB respectively across the whole tilting range. Having the advantage of simple structure and compact size, easy assembly and high reliability, as well as the outstanding performance, the proposed antenna and its array will contribute well to the applications in the current 4G LTE and future 5G wireless communication systems.

ACKNOWLEDGMENT

This work was supported by Amphenol Antenna Solutions, Inc. 1123 Industrial Dr. SW, Conover, NC 28613, USA, with a US patent pending (Application No. 15/250,481).

REFERENCES

1. Lindmark, B. and M. Nillson, "On the available diversity gain from different dual-polarized antennas," *IEEE Journal on Selected Areas in Communications*, Vol. 19, No. 2, 287–294, Feb. 2001.
2. Gou, Y., S. Yang, Q. Zhu, and Z. Nie, "A compact dual-polarized double E-shaped patch antenna with high isolation," *IEEE Trans. Antennas Propag.*, Vol. 61, No. 8, 4349–4353, Aug. 2013.
3. Bao, Z., Z. Nie, and X. Zong, "A novel broadband dual-polarization antenna utilizing strong mutual coupling," *IEEE Trans. Antennas Propag.*, Vol. 62, No. 1, 450–454, Jan. 2014.

4. Cui, Y.-H., R. Li, and H. Fu, "A broadband dual-polarized planar antenna for 2G/3G/LTE base stations," *IEEE Trans. Antennas Propaga.*, Vol. 62, No. 9, 4836–4840, Sep. 2014.
5. Chu, Q., D. Wen, and Y. Luo, "A broadband ±45° dual-polarized antenna with Y-shaped feeding lines," *IEEE Trans. Antennas Propaga.*, Vol. 63, No. 2, 483–490, Feb. 2013.
6. Li, R., T. Wu, B. Pan, K. Lim, J. Lasker, and M. Tentzeris, "Equivalent circuit analysis of a broadband printed dipole with adjusted integrated balun and an array for base station applications," *IEEE Trans. Antennas Propaga.*, Vol. 57, 2180–2184, Jul. 2009.
7. Zhou, Z., S. Yang, and Z. Nie, "A novel broadband printed dipole antenna with low cross-polarization," *IEEE Trans. Antennas Propaga.*, Vol. 55, 3091–3093, Nov. 2007.
8. He, Q., B. Wang, and J. He, "Wideband and dual-band design of a printed dipole antenna," *IEEE Antennas Wireless Propag. Lett.*, Vol. 7, 1–4, 2008.
9. Liu, Y., H. Yi, F.-W. Wang, and S.-X. Gong, "A novel miniaturized broadband dual-polarized dipole antenna for base station," *IEEE Antennas Wireless Propag. Lett.*, Vol. 12, 1335–1338, 2013.
10. Wu, J., Z. Zhao, Z. Nie, and Q. Liu, "A compact printed dipole antenna for wideband wireless applications," *Progress In Electromagnetics Research C*, Vol. 50, 95–102, 2014.
11. Gou, Y., S. Yang, J. Li, and Z. Nie, "A compact dual-polarized printed dipole antenna with high isolation for wideband base station applications," *IEEE Trans. Antennas Propaga.*, Vol. 62, No. 8, 4392–4395, Aug. 2014.
12. Huang, H., Y. Liu, and S. Gong, "A novel dual-broadband, dual-polarized antenna for 2G/3G/LTE base stations," *IEEE Trans. Antennas Propaga.*, Vol. 64, No. 9, 4113–4118, 2016.
13. HFSS: High Frequency Structure Simulator Based on the Finite Element Method Ansoft Corp.
14. Tang, T. G., Q. M. Tieng, and M. W. Gunn, "Equivalent circuit of a dipole antenna using frequency-independent lumped elements," *IEEE Trans. Antennas Propaga.*, Vol. 41, No. 1, 100–103, Jan. 1993.
15. D'Aquino, A., "Recommendation on base station antenna standards by NGMN alliance, N-P-BASTA," Version 10.0, Dec. 2016.
16. Janaswamy, R., "Effects of mutual coupling on the capacity of fixed length linear arrays," *IEEE Antennas Wireless Propag. Lett.*, Vol. 1, 157–160, 2002.
17. Oh, T., Y.-G. Lim, C.-B. Chae, and Y. Lee, "Dual-polarization slot antenna with high cross-polarization discrimination for indoor smallcell MIMO systems," *IEEE Antennas Wireless Propag. Lett.*, Vol. 14, 374–377, 2015.
18. Zheng, W. C., L. Zhang, Q. X. Li, and Y. Leng, "Dual-band dual-polarized compact bowtie antenna array for anti-interference MIMO WLAN," *IEEE Trans. Antennas Propag.*, Vol. 62, No. 1, 237–246, Jan. 2014.
19. Donelli, M. and P. Febvre, "An inexpensive reconfigurable planar array for Wi-Fi applications," *Progress In Electromagnetic Research C*, Vol. 28, 71–81, 2012.
20. Votis, C., G. Tatsis, and P. Kostarakis, "Envelope correlation parameter measurements in a MIMO antenna array configuration," *Int. J. Commun., Netw. Syst. Sci.*, Vol. 2, No. 4, 350–354, 2010.
21. Vaughan, R. G. and J. B. Andersen, "Antenna diversity in mobile communications," *IEEE Transactions on Vehicular Technology*, Vol. 36, 149–172, 1987.
22. Arun, H., A. K. Sarma, M. Kanagasabai, S. Velan, C. Raviteja, and M. G. N. Alsath, "Deployment of modified serpentine structure for mutual coupling reduction in MIMO antennas," *IEEE Antennas Wireless Propag. Lett.*, Vol. 13, 277–280, 2014.
23. Alsath, M. G. N., M. Kanagasabai, and B. Balasubramanian, "Implementation of slottedmeander-line resonators for isolation enhancement in microstrip patch antenna arrays," *IEEE Antennas Wireless Propag. Lett.*, Vol. 12, 15–18, 2013.
24. Massa, A., M. Donelli, F. De Natale, S. Caorsi, and A. Lommi, "Planar antenna array control with genetic algorithms and adaptive array theory," *IEEE Trans. Antennas Propag.*, Vol. 52, 2919–2924, Nov. 2004.
25. Donelli, M., S. Caorsi, F. De Natale, D. Franceschini, and A. Massa, "A versatile enhanced genetic algorithm for planar array design," *Journal of Electromagnetic Waves and Applications*, Vol. 18, No. 11, 1533–1548, Nov. 2004.